Cite as: J. Appl. Phys. 133, 225304 (2023); doi: 10.1063/5.0147124 Submitted: 19 February 2023 · Accepted: 24 May 2023 · Published Online: 12 June 2023







H. Alex Hsain,<sup>1,2,a)</sup> (D) Younghwan Lee, <sup>1</sup> (D) Patrick D. Lomenzo, <sup>2</sup> (D) Ruben Alcala, <sup>2</sup> (D) Bohan Xu, <sup>2</sup> (D) Thomas Mikolajick.<sup>2,3</sup> 📵 Uwe Schroeder.<sup>2</sup> 📵 Gregory N. Parsons.<sup>4</sup> 📵 and Jacob L. Jones<sup>1,a)</sup> 📵

Thomas Mikolajick, 2.3 © Uwe Schroeder, 2 © Gregory N. Parsons, 4 © and Jacob L. Jones 1.a) ©

AFFILIATIONS

1 Department of Materials Science and Engineering, North Carolina State University, 911 Partners Way, Raleigh, North Carolina 27695, USA

2 NaMLab gGmbH, Nöthnitzer Strasse 64a, Dresden 01187, Germany

3 TU Dresden, Chair of Nanoelectronics, Nöthnitzer Strasse 64a, 01187 Dresden, Germany

4 Department of Chemical and Biomolecular Engineering, North Carolina State University, 911 Partners Way, Raleigh, North Carolina 27695, USA

3 Authors to whom correspondence should be addressed: hahsain@ncsu.edu and jacobjones@ncsu.edu

ABSTRACT

Ferroelectric hafnium-zirconium oxide (HZO) is an excellent candidate for low-power non-volatile memory applications due to its demonstrated ferroelectricity at the nanoscale and compatibility with silicon-based technologies. The interface of HZO in contact with its electrode, typically TiN in a metal-ferroelectric—metal (MFM) capacitor configuration, is of particular interest because factors, such as volume confinement, impurity concentration, interfacial layers, thermal expansion mismatch, and defect trapping, are believed to play a crucial role in the ferroelectric performance of HZO-based devices. Processing variables, such as precursor type, oxygen source, dose duration, and deposition temperature, are known to strongly affect the quality of the oxide-metal interface. However, not many studies have focused on the effect of breaking or maintaining vacuum during MFM deposition. In this study, sequential, no-atmosphere processing (SNAP) is employed to avoid atmospheric exposure, where electrode TiN and ferroelectric HZO are deposited sequentially in the atomic layer deposition chamber without breaking vacuum. The effect of breaking vacuum during the sequential deposition steps is elucidated by fabricating and characterizing MFM capacitors with and without intentional vacuum breaks prior to the deposition of the HZO and top TiN. Using x-ray photoelectron spectroscopy and time electrode deposition leads to interfacial oxidation and increased carbon contamination, which preferentially stabilizes the non-ferroelectric eteragonal phase and lead to diminished remanent polarization. Avoiding carbon impurities and lead to diminished remanent polarization. face using SNAP leads to heightened remanent polarization. Avoiding carbon impurities and interfacial TiO<sub>x</sub> at the HZO and TiN interface using SNAP leads to heightened remanent polarization, reduced leakage current density, and elimination of the wake-up effect. Our book highlights the effect of vacuum breaking on the processing-structure-properties of HZO book and the structure of the processing structure properties of HZO book and the structure of the processing structure properties of HZO book and the processing structure properties of the processing structure properties of HZO book and the processing structure properties of the processing structure properties of the processing structure properties of the processing structure proper vacuum can significantly improve ferroelectric properties.

Published under an exclusive license by AIP Publishing. https://doi.org/10.1063/5.0147124

### I. INTRODUCTION

An interface is formed at the boundary of two dissimilar materials, e.g., oxide-metal, and can strongly govern the resulting structure and properties of a device, especially when the structure is only a few tens of nanometers thick, such as the case of HZO-based capacitors. In practice, it is not only the choice of the

materials that determine the interface characteristics but also the choice of processing conditions during fabrication. Understanding the processing-structure-properties in oxide-metal interfaces is essential in leveraging the full capabilities of materials.

Doped hafnia (HfO<sub>2</sub>)<sup>1</sup> and HZO<sup>2</sup> thin films have emerged as attractive candidates for ferroelectric device applications because of

their ability to demonstrate ferroelectricity at the nanoscale and compatibility with complementary metal-oxide-semiconductor (CMOS) technology. Given the loss thickness of HZO thin films of 10 nm or below in device applications, the interface plays an even more crucial role in achieving ferroelectric polarization and its stability compared to traditional perovskite ferroelectrics. Defects at the interface can cause polar discontinuities and lead to loss of polarization and device functionality.3 Many studies have found that engineering the electrode-oxide interface can directly control the microstructure and ferroelectric properties of HZO thin Conventional HZO-based metal-ferroelectric-metal (MFM) structures most often utilize TiN as the top and bottom electrodes forming the HZO/TiN interface.<sup>8,9</sup> TiN is typically deposited via physical vapor deposition (PVD) whereas the HZO is deposited via atomic layer deposition (ALD). It is inevitable to break vacuum when transferring a sample from a PVD chamber to an ALD chamber to complete the entire MFM stack. Thus, the exposed surface of TiN will naturally oxidize, and adventitious hydrocarbons will adhere to the surface during the exposure to the ambient atmosphere and partially decompose to carbon before HZO deposition. Among other effects, the native oxide and adventitious carbon may act as a dead layer which could add unwanted capacitance in series in the device. Therefore, it is critical to understand the effect of ambient atmosphere exposure to the device performance and, if possible, find a way to mitigate the atmosphere exposure.

Recent studies have investigated the impact of processing conditions on the chemistry of HZO interface in contact with its metal electrode. Filatova et al. used Hard X-ray Photoelectron Spectroscopy (HAXPES) to reveal the chemistry at the interface of HfO2 and TiN. The interface of ALD-based HfO2 on top of PVD-based TiN showed signatures of TiO2 and TiNxOv throughout an approximately 2.7 nm thick interfacial region. Filatova et al. suggested that interlayers formed via either TiN scavenging oxygen from HfO2 or the direct oxidation of TiN by the oxygen source species used during ALD of the HfO2 layer on top of TiN. Another HAXPES study by Szyjka et al. suggested that the oxygen vacancy concentration in PVD-fabricated TiN/HfO2/TiN devices could be altered by flowing oxygen gas either during or before deposition of HfO<sub>2</sub>. The pre-flow of oxygen could stabilize the TiN/HfO<sub>2</sub> interface via formation of a TiO2 interfacial layer. Another studying employing TEM revealed that a strong orientational alignment forms between hafnia and zirconia with TiN electrodes. 10 A thicker interface has been found to reduce the crystallite alignment between the HZO and the bottom interface, accordingly changing the phase formation in the ferroelectric layer. The symmetry of top and bottom electrode interfaces can also impact device properties. Lomenzo et al. showed that chemical heterogeneity of the top and bottom interface in TaN/HZO/TaN capacitors gave rise to an internal electric field, which caused preferential polarization of ferroelectric domains in one direction.<sup>4</sup> The asymmetrical distribution of space charge at top and bottom electrodes was detrimental due to the instability of one of the polarization states. Lomenzo et al. suggested that in situ ALD electrode deposition would be a viable way to avoid electrode oxidation and contamination, thereby improving the symmetry of the electrode-oxide interface. In situ ALD would not only avoid oxidation of the bottom interface but

could also lead to a reduction in carbon impurities which has been shown to influence the ferroelectric properties of HZO.

Previously, we demonstrated the merit of fully ALD-grown metal-ferroelectric-metal (MFM) capacitors of TiN/HZO/TiN using a process called sequential no-atmosphere processing (SNAP). SNAP involves sequential deposition of all three layers (electrode, ferroelectric, electrode) in the same chamber without the breaking of vacuum. SNAP-fabricated capacitors exhibited more chemically pristine interfaces and unexpectedly high remanent polarization. In the present work, to more fully characterize the effect of vacuum breaking during the sequential deposition steps, an MFM device is fabricated with intentional vacuum breaks prior to the deposition of the HZO and the top TiN, which, herein, is referred to as non-SNAP. The non-SNAP capacitors are then compared and contrasted to those fabricated via SNAP. Furthermore, the development of native oxidation and adventitious carbon on the non-SNAP-fabricated capacitors is characterized and the consequences on the structural and electrical properties in ferroelectric HZO are studied in detail. We report chemical and structural property differences between films using X-ray Photoelectron for the Secondary Ion Mass Spectroscopy (XPS), Time-of-Flight Secondary Ion Mass Spectrometry (ToF-SIMS), and Grazing Incidence X-ray Diffraction (GIXRD). We show that SNAP-fabricated capacitors exhibit a 30% increased remanent polarization and virtually no wake-up effect. We ascribe the enhanced ferroelectric properties in SNAP-fabricated capacitors to the vacuum-maintaining ALD procedure, which minimizes interfacial oxidation and hydrocarbon

impurities.

II. METHODS

The MFM stack was composed from bottom to top: Si wafer/
30 nm TiN/10 nm HZO/10 nm TiN and was deposited sequentially without breaking vacuum during ALD (Ultratech/Cambridge Fiji)

G2) using the sequential, no-atmosphere processing (SNAP)<sup>12</sup>

The sequential of the sequential to the sequential of the sequenti procedure. The precursors used for this process were tetrakis(dimethylamido)-hafnium(IV) (TDMAH), tetrakis(dimethylamido)-zir- conium(IV) (TDMAZ), and tetrakis(dimethylamido)-titanium(IV) thylamido)-hafnium(IV) (TDMAH), tetrakis(dimethylamido)-zir-(TDMAT), and water (H<sub>2</sub>O) as the oxygen source. The temperature for all precursors, delivery line, and chamber was maintained at 75, and 270 °C, respectively. The ALD temperature of 270 °C was selected since it lies in the middle of the ALD window for all pre-cursors and has shown to result in the lowest film resistivity for TiN.<sup>13</sup> TiN deposition was accomplished via plasma-enhanced <sup>72</sup> ALD using 250 W plasma power for a period of 20 s, where 430 g cycles were pulsed at a growth rate of ~0.6 Å/cycle. A gas flow of 110 sccm Ar was used to deliver the precursors into the ALD chamber and Ar:N2 of 10:20 sccm was used to generate plasma for TiN deposition. The stoichiometric ratio of Ti to N was confirmed to be approximately 1:1 and XRD revealed that the TiN film was 001-textured. For thermal ALD of HZO, Hf/Zr precursors were pulsed for  $0.25 \, s$  followed by a  $5 \, s$  purge time, and then  $0.1 \, s$   $H_2O$ was pulsed followed by a 5 s purge time. Alternating cycles of Hf and Zr precursors were pulsed for 100 cycles with an approximate growth rate of 1.0 Å/cycle to obtain a 1:1 composition of an approximately ~10 nm HZO thin film. The thickness was confirmed via ellipsometry with a standard model for HZO and TiN,

**TABLE I.** XPS survey scan quantification of atomic concentration of various chemical species on the surface of TiN after two exposure times.

	C 1s (at. %)	O 1s (at. %)	Ti 2p (at. %)	N 1s (at. %)
Fresh	$20.4 \pm 0.3$	$21.1 \pm 0.3$	$26.2 \pm 0.2$	$32.3 \pm 0.4$
24 h	$22.3 \pm 0.3$	$24.5 \pm 0.3$	$24.0 \pm 0.2$	$29.2 \pm 0.3$

and XPS revealed a 1:2 ratio of Hf/Zr to O. MFM structures were then annealed via rapid thermal annealing (AnnealSys AS-One) with a ramp rate of  $10\,^{\circ}$ C/s to 400, 600, and  $800\,^{\circ}$ C with a hold time of  $30\,^{\circ}$ S.

Non-SNAP films were processed via an identical ALD recipe but with intentional vacuum breaking steps after each layer deposition. Specifically, after the deposition of each sequential layer, i.e., the bottom TiN and HZO layer, non-SNAP films were taken out of the ALD chamber and exposed to the ambient cleanroom environment at room temperature for 24 h. MFM capacitors were subsequently annealed at 400, 600, or 800  $^{\circ}$ C for 30 s in N<sub>2</sub>.

For electrical characterization, 200 µm contact pads of 10 nm Ti/30 nm Pt were deposited via e-beam evaporation through a shadow mask. MFM samples were subsequently etched using a standard SC1 etch H<sub>2</sub>O:H<sub>2</sub>O<sub>2</sub>:NH<sub>3</sub> 50:2:1 at 50 °C for 5 min. Ferroelectric characterization was conducted using an aixACCT System TF Analyzer 3000, where each measurement was performed on a pristine contact with no previous electrical history. For polarization-electric field (P-E) measurements, bipolar electric fields were utilized with triangular waveforms, a frequency of 1 kHz, and maximum electric field amplitudes between 1 and 4 MV/cm. Endurance was tested using a bipolar square waveform with 100 kHz frequency and maximum electric field amplitude of either 3 or 3.5 MV/cm, during which P-E measurements were taken five times per decade on a log-scale. Capacitance vs DC bias offset voltage (C-V) was measured using a bipolar 50 mV small-signal amplitude at 10 kHz and DC bias offset voltages up to 3 V. Experimental details for GIXRD, XPS, and ToF-SIMS characterization are found in the supplementary material.

## III. RESULTS AND DISCUSSION

In the case of the non-SNAP fabrication procedure, a 30 nm layer of TiN is grown via ALD and then taken out of the ALD chamber and exposed to the ambient cleanroom environment for 24 h; this exposure process is expected to promote oxide growth and carbon adsorption. To elucidate the chemical changes on the TiN surface in response to vacuum breaking during fabrication, a 30 nm TiN film was exposed to two different air exposure durations: immediately after deposition, i.e., "fresh," and 24 h. The chemical properties of ALD-grown TiN with and without air exposure are investigated via XPS where C 1s, O 1s, Ti 2p, and N 1s species were quantified in atomic concentration from a survey scan for fresh and 24 h air exposure TiN films (Table I). Note that the carbon concentration determined by XPS is not only due to the presence of unreacted ligands from ALD metalorganic precursors but also accounts for adsorbed hydrocarbons from exposure to the atmosphere. The XPS quantification is consistent with previous depth profiling XPS work which suggested  $\sim$ 20 at. % C on the surface of the film which decreases to <5 at. % when measured within the MFM stack. Though the carbon concentration is high in both samples, the sample exposed to atmosphere for 24 h shows a  $\sim$ 2 at. % higher carbon concentration, consistent with the hypothesis that vacuum breaking leads to higher adsorption of adventitious carbon from the atmosphere. Additionally, the oxygen concentration increases by over 4 at. % while titanium and nitrogen decrease by several atomic percent, consistent with the thermodynamically favorable oxidation reaction of TiN.  $^{14}$ 

High-resolution spectra of C 1s, O 1s, Ti 2p, and N 1s were also acquired to elucidate the differences in bonding states between fresh and 24 h exposed TiN and are shown in Fig. 1. Figure 1(a) shows the C 1s high-resolution spectra for fresh and 24 h exposed TiN. The peak intensity corresponding to C-C bonds is located at 285 eV and shows an increase for TiN after 24 h exposure, consistent with the higher carbon concentration shown in the survey scan quantification. Figure 1(b) shows the O 1s high-resolution spectra for both films where the increase in peak intensity, specifically at  $\frac{m}{2}$ the binding energies corresponding to C-O/Ti-O (530 eV) and a Ti-O-N/C-O-C (532 eV), which likely stems from the thermodynamically favored oxidation of TiN upon air exposure and the interaction of oxygen with adsorbed hydrocarbon. Similar trends are observed in the high-resolution spectra of Ti 2p in Fig. 1(c) where the diminished intensity of the Ti-N peaks at 463 and 5 457 eV correspond to a decrease in TiN concentration in favor of TiO<sub>x</sub> growth. Figure 1(d) shows the high-resolution spectra of N 1s where the peak decreases in intensity in TiN after 24 h of exposure, consistent with a reduced fraction of Ti-N bonds. The XPS analysis presented here indicates that vacuum breaking and exposure for \$\frac{b}{24}\$ h to ambient air promotes adsorption of adventitious carbon and small amounts of TiN oxidation.

To study the impact of vacuum breaking during ALD on MFM chemical interfaces, non-SNAP- and SNAP-fabricated TiN/HZO/TiN capacitors were evaluated via ToF-SIMS depth profiling shown in Figs. 2(a) and 2(b). For these tests, capacitors were prepared and annealed in N<sub>2</sub> for 30 s at 400, 600, and 800 °C before depth profiling. Chemical species of ZrO<sub>2</sub>, HfO<sub>2</sub>, C<sub>2</sub>, CN<sup>-</sup>, Qf<sup>47</sup>TiN<sup>-</sup>, and <sup>50</sup>TiO<sup>-</sup> are shown to compare their relative quantities and distribution within the two MFM stacks. For all annealing temperatures, both capacitors show an increase in HfO<sub>2</sub> and ZrO<sub>2</sub> observed in the middle of the capacitor stack at 150–250 s sputtering depth and an increase in <sup>47</sup>TiN<sup>-</sup> intensity at 0–100 s and 300–600 s sputtering depth, consistent with the expected TiN/HZO/TiN arrangement of the capacitor stack.

For all annealing temperatures, the most significant differences between the non-SNAP- and SNAP-fabricated samples are observed for  $C_2^ CN^-$ , and  $^{47}\text{TiN}^-$  species. Specifically, the  $C_2^-$  species showed a significantly heightened concentration at the bottom HZO/TiN interface at 200–300 s sputtering depth within the non-SNAP capacitor. To better quantify the difference in carbon impurities between non-SNAP and SNAP capacitors, the ratio of  $C_2^-$  to  $HfO_2^-$  species is plotted in Fig. 3 at the sputtering depth that corresponds to the bottom HZO/TiN interface. The higher  $C_2^-$  to  $HfO_2^-$  ratio in the non-SNAP-fabricated capacitor is consistent with the hypothesis that vacuum breaking introduces more organic volatiles to the interface.

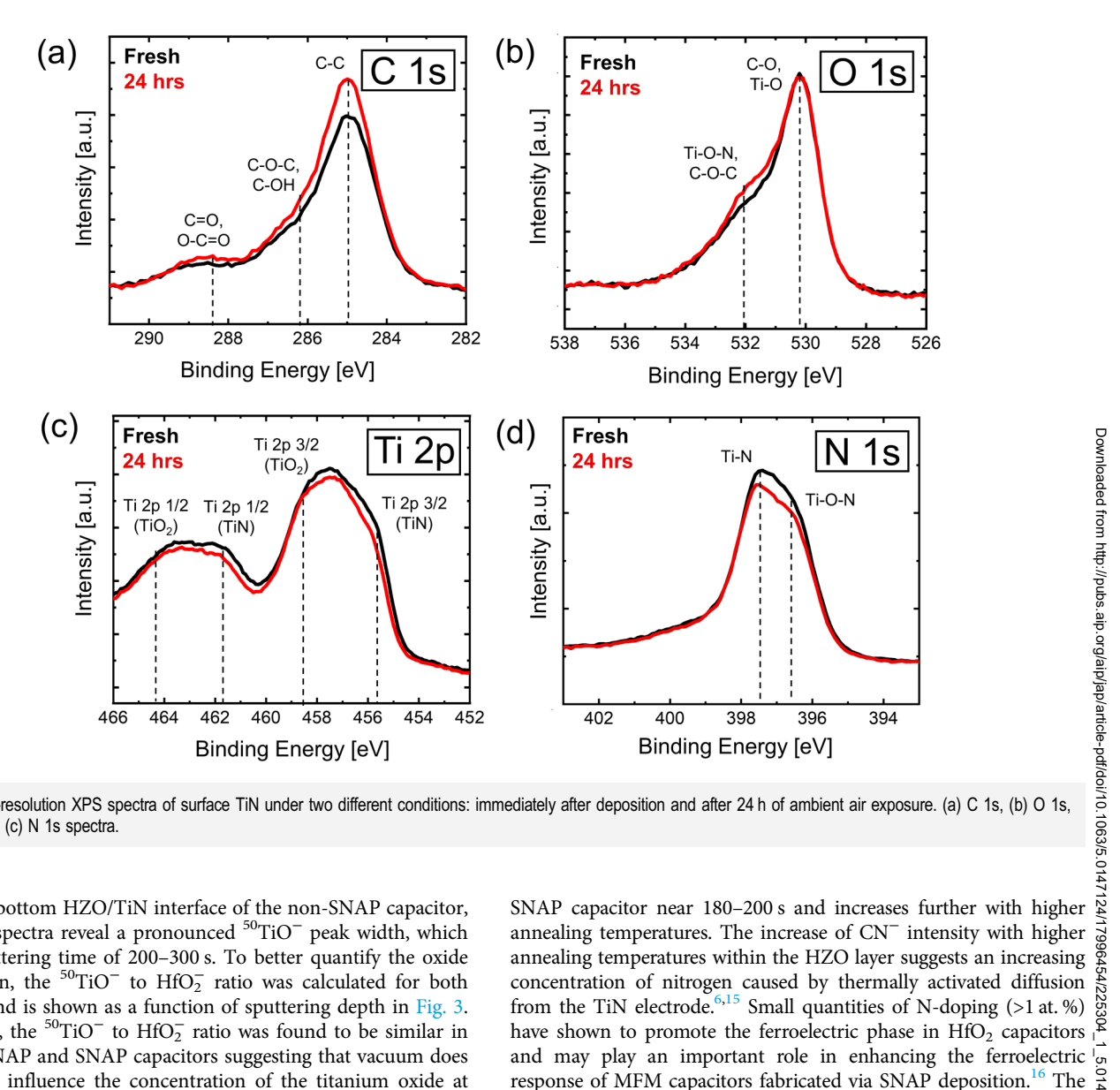


FIG. 1. High-resolution XPS spectra of surface TiN under two different conditions: immediately after deposition and after 24 h of ambient air exposure. (a) C 1s, (b) O 1s, (c) Ti 2p, and (c) N 1s spectra.

At the bottom HZO/TiN interface of the non-SNAP capacitor, the <sup>50</sup>TiO<sup>-</sup> spectra reveal a pronounced <sup>50</sup>TiO<sup>-</sup> peak width, which spans a sputtering time of 200-300 s. To better quantify the oxide concentration, the <sup>50</sup>TiO<sup>-</sup> to HfO<sub>2</sub> ratio was calculated for both capacitors and is shown as a function of sputtering depth in Fig. 3. Interestingly, the <sup>50</sup>TiO<sup>-</sup> to HfO<sub>2</sub> ratio was found to be similar in both non-SNAP and SNAP capacitors suggesting that vacuum does not strongly influence the concentration of the titanium oxide at the bottom interface. The analysis was repeated for the top interface found at a sputtering time of 110-130 s in Fig. S2 in the supplementary material and similar trends were observed. The TOF-SIMS analysis was cross-checked with HAADF measurements shown in Fig. S1 in the supplementary material, which confirmed similar levels of interfacial oxidation. In combination, these data suggest that both non-SNAP and SNAP-fabricated capacitors were found to form similar interfacial oxides due to the spontaneous oxidation reaction between TiN and HZO.

The ToF-SIMS spectra of the SNAP-fabricated capacitor in Fig. 2(b) reveal potential nitrogen incorporation in HZO. Though the intensity of the C<sub>2</sub> signal decreases in the middle of the HZO layer and stays relatively constant across all annealing temperatures, the intensity of the CN intensity is significantly higher in the and may play an important role in enhancing the ferroelectric response of MFM capacitors fabricated via SNAP deposition. <sup>16</sup> The lower nitrogen concentration in the non-SNAP capacitor may be <sup>17</sup>/<sub>24</sub> due to carbon impurities or TiO<sub>x</sub> and TiO<sub>x</sub>N<sub>y</sub> species, which can get as diffusion barriers. 6,17,18 Energy Dispersive Spectroscopy (EDS) (Fig. S1 in the supplementary material) was conducted to investigate the differences in TiOx interfacial oxidation and N concentration. Higher N counts were found in the HZO layer of SNAP-fabricated capacitors, in agreement with evidence of N-doping found in depth profiling TOF-SIMS. The EDS spectra did not show any appreciable differences in the interfacial oxidation of non-SNAP- and SNAP capacitors consistent with ToF-SIMS quantification from Fig. 3. In summary, chemical analysis reveals that breaking vacuum during ALD of TiN/HZO/TiN does not strongly influence the oxidation behavior at the interface but primarily leads to the deposition of adventitious hydrocarbons from the air.

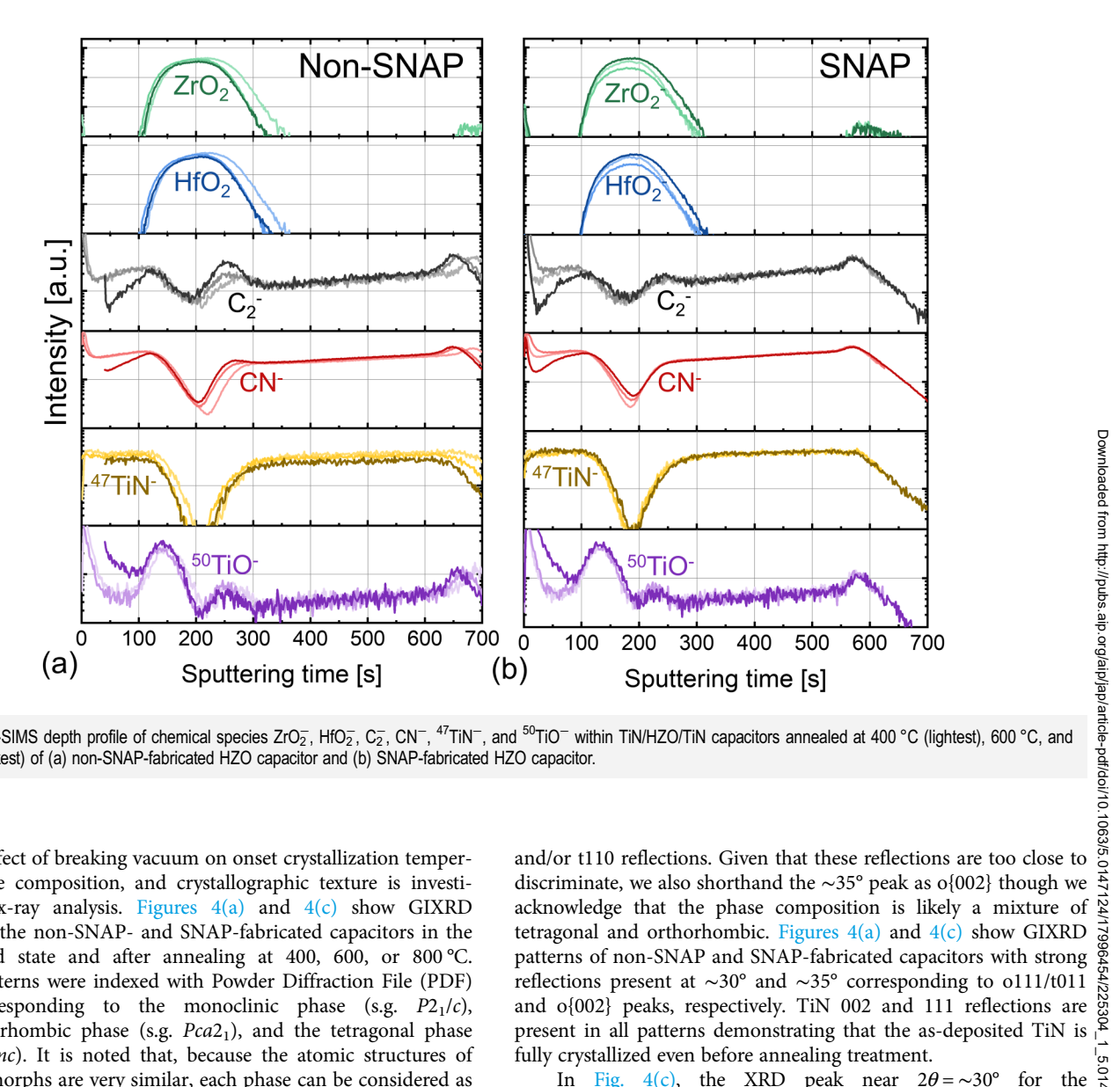


FIG. 2. ToF-SIMS depth profile of chemical species ZrO<sub>2</sub>, HfO<sub>2</sub>, C<sub>2</sub>, CN<sup>-</sup>, <sup>47</sup>TiN<sup>-</sup>, and <sup>50</sup>TiO<sup>-</sup> within TiN/HZO/TiN capacitors annealed at 400 °C (lightest), 600 °C, and 800 °C (darkest) of (a) non-SNAP-fabricated HZO capacitor and (b) SNAP-fabricated HZO capacitor.

The effect of breaking vacuum on onset crystallization temperature, phase composition, and crystallographic texture is investigated via x-ray analysis. Figures 4(a) and 4(c) show GIXRD patterns of the non-SNAP- and SNAP-fabricated capacitors in the as-deposited state and after annealing at 400, 600, or 800 °C. GIXRD patterns were indexed with Powder Diffraction File (PDF) cards corresponding to the monoclinic phase (s.g.  $P2_1/c$ ), polar orthorhombic phase (s.g. Pca21), and the tetragonal phase (s.g. P42/nmc). It is noted that, because the atomic structures of HZO polymorphs are very similar, each phase can be considered as a small distortion from a shared cubic parent phase, or what can be called a pseudo-cubic reference frame. The XRD patterns of polymorphs that are similar share many similar XRD reflections. For example, the d-spacing of both {111} planes of the polar orthorhombic phase and (101) planes of the tetragonal phase are similar (2.9-3.0 Å), which correspond to the XRD reflections of maximum relative intensity at  $2\theta = \sim 30^{\circ}$ . Thus, the XRD peak that appears near  $2\theta = \sim 30^{\circ}$  can be interpreted as either the 111 reflection of the orthorhombic phase (referred to here as o111), the 101 reflection of the tetragonal phase (referred to here as t101), or a combination of these reflections. Since these two reflections are too close to be resolved, the peak in this region is referred to as the o111/t011 peak. Consistently, the XRD peak that appears near  $2\theta = \sim 35^{\circ}$  may be also understood as a combination of o002, o020, o200, t002,

fully crystallized even before annealing treatment.

fully crystallized even before annealing treatment.

In Fig. 4(c), the XRD peak near  $2\theta = \sim 30^{\circ}$  for the SNAP-fabricated capacitor emerges at 400 °C, while the same peak  $20^{\circ}$ for the non-SNAP capacitor does not noticeably appear until 600 °C & in Fig. 4(a), indicating that the onset crystallization temperature of the SNAP-fabricated capacitor is lower than that of the non-SNAP capacitor. Given that the thickness of both HZO films was confirmed as ~10 nm via ellipsometry and Transmission Electron Microscopy (TEM), the difference in onset crystallization likely stems from the characteristics of the bottom HZO/TiN interface. Studies have shown that the composition and crystallinity of an underlying layer can subsequently affect film crystallinity and phase composition of the overlying film. 19-21 Park et al. showed that ZrO2-starting HZO nanolaminates formed larger as-deposited crystallites and subsequently resulted in a higher degree of crystallinity in as-deposited films. 19 Consistently, Ho et al. also showed that the

morphology and crystallization kinetics of ALD HfO2 was strongly influenced by the crystallinity of the underlying SiO<sub>2</sub> layer. Oiven that the bottom TiN electrode in the present study is highly crystallized as-deposited, grains of TiN in direct contact with HZO may provide a heterogeneous nucleation site for the crystallization of HZO at lower temperatures when films are grown without vacuum breaking steps. On the other hand, breaking vacuum during ALD leads to the interfacial carbon, which inhibits direct contact with the underlying TiN and may increase the thermal energy required to activate film crystallization.

A non-negligible peak shift toward lower  $2\theta$  with increasing annealing temperature was also observed for both non-SNAP- and SNAP-fabricated samples shown in Figs. 4(b) and 4(d), respectively, and likely corresponds to a phase transformation from the non-polar tetragonal to the polar orthorhombic phase. 22,23 It should be noted that the  $2\theta$  positions of the maximum intensity peak of the polar orthorhombic and tetragonal phases of HZO are expected to appear near  $2\theta = 29.9^{\circ}$  and  $2\theta = 30.3^{\circ}$ , respectively. Thus, a peak shift toward lower  $2\theta$  with increasing annealing temperature is consistent with an increase in orthorhombic phase fraction.<sup>22</sup> From 600 to 800 °C, the oll1/t011 reflection peak shifts from 30.80° to 30.65° for the non-SNAP capacitor and from 30.80° to 30.50° for the SNAP capacitor. The blue and red stripes in Figs. 4(b) and 4(d) correspond to the peak shift of  $\Delta 2\theta = \sim 0.15^{\circ}$ and  $\Delta 2\theta = \sim 0.30^{\circ}$  for the non-SNAP and SNAP capacitor, respectively. The larger  $\Delta 2\theta$  upon annealing seen in the SNAP capacitor suggests that maintaining vacuum during ALD results in films with a higher fraction of the polar orthorhombic phase. On the other hand, the higher  $2\theta$  position of the o111/t011 peak at all annealing temperatures in the non-SNAP capacitor are consistent with a higher tetragonal phase composition if a constant stress/strain is assumed for the films. The high tetragonal phase fraction in non-SNAP can be attributed to the higher concentration of carbon impurities as carbon has been shown to suppress ferroelectric properties in HZO films.2

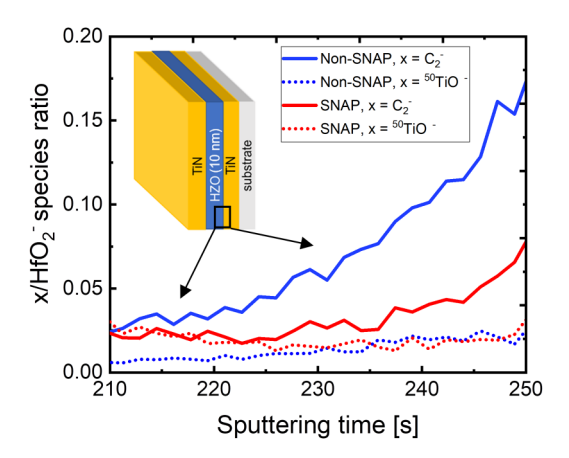


FIG. 3. ToF-SIMS ratio of C<sub>2</sub> and <sup>50</sup>TiO<sup>-</sup> to HfO<sub>2</sub> species at the TiN/HZO bottom interface for non-SNAP-fabricated and SNAP-fabricated films annealed at 800 °C.

It is also interesting to note the slight normalized intensity differences of the o111/t011 and o{002} peak in non-SNAP- and SNAP-fabricated capacitors. Given the higher degree of o111/t011 peak shift in SNAP-fabricated capacitors, the lowered o111/t011 peak intensity does not likely stem from a lower orthorhombic phase fraction. Instead, the higher relative intensity of the o{002} peak compared to o111/t011 might suggest a preferred 001-texture. A semi-quantitative texture analysis was performed where each o111/t011 and o{002} peak was fit to an asymmetric Pearson-VII model profile shape function using LIPRAS software.<sup>25</sup> Figure S3 in the supplementary material shows that the [o111/t011]/o{002} ratio increases as a function of annealing temperature for non-SNAP-fabricated capacitors while the [o111/t011]/o{002} ratio decreases linearly in the SNAP capacitor. Given the strong 001-texture of the TiN used in this study, a texture inheritance effect may occur between HZO and the underlying TiN, which could promote the growth of 100, 010, and/or 001 HZO poles that are aligned normal to the film, leading to a higher remanent polarization. The aforementioned hypothesis is further supported by Lee et al., in which the TiN crystallographic texture was found to influence structural and electrical properties of HZO films.<sup>26</sup> In the non-SNAP capacitor, the HZO and TiN interface is disrupted because of the more pronounced interfacial layer, breaking the way in which texture can be related or inherited from the substrate to the HZO film and lead to a higher o111/t011 peak intensity relative the HZO film and lead to a higher o111/t011 peak intensity relative of to o{002}. In summary, GIXRD analysis suggests that vacuum breaking during ALD fabrication of TiN/HZO/TiN capacitors has the potential to influence the onset crystallization of HZO, phase composition, and crystallographic texture in the HZO films.

Figure 5 shows the room-temperature polarization and leakage current measurements of non-SNAP and SNAP-fabricated capacitors after deposition and annealing at 800 °C for 30 s. Electrical measurements for non-SNAP and SNAP-fabricated capacitors annealed at 400 and 600 °C are also shown in Fig. S4 in the supplementary material. Since capacitors annealed at 800 °C showed the most prominent ferroelectricity, they were selected for subsequent analysis. P-E loops are displayed in Fig. 5(a), where the remanent  $\frac{1}{2}$  polarization ( $P_T$ ) value is extracted at 0 MV/cm. Overlaying the P-  $\frac{1}{2}$ polarization (P<sub>r</sub>) value is extracted at 0 MV/cm. Overlaying the P-E loops is the current density vs electric field (J-E). The P<sub>r</sub> values were measured to be 17 and  $23 \mu \text{C/cm}^2$  for non-SNAP and SNAP capacitors, respectively. The higher Pr value and the unpinched P-E loop found in the SNAP capacitor is consistent with a higher orthorhombic phase fraction evidenced by x-ray analysis. At the same time, the pinched hysteresis and double peak in the J-E curve 72. of the non-SNAP capacitor is consistent with a higher tetragonal g phase fraction composition evidenced by GIXRD analysis.

Several factors support the formation of the orthorhombic phase in HZO fabricated via SNAP including (1) the mitigation of interfacial layer development which is known to elicit a depolarization field<sup>27,28</sup> and (2) the diffusion of N atoms into the HZO layer which has been correlated with stabilizing the orthorhombic phase even in small concentrations. Xu et al. showed that only a 0.34% N concentration was enough to induce a switchable polarization of  $21 \,\mu\text{C/cm}^2$ . In the HZO film processed with vacuum breaking steps, however, the P-E loop shows a distinct "pinching" near the coercive field which could be caused by domain pinning,<sup>29</sup> non-ferroelectric interface, or a ferroelectric and paraelectric phase

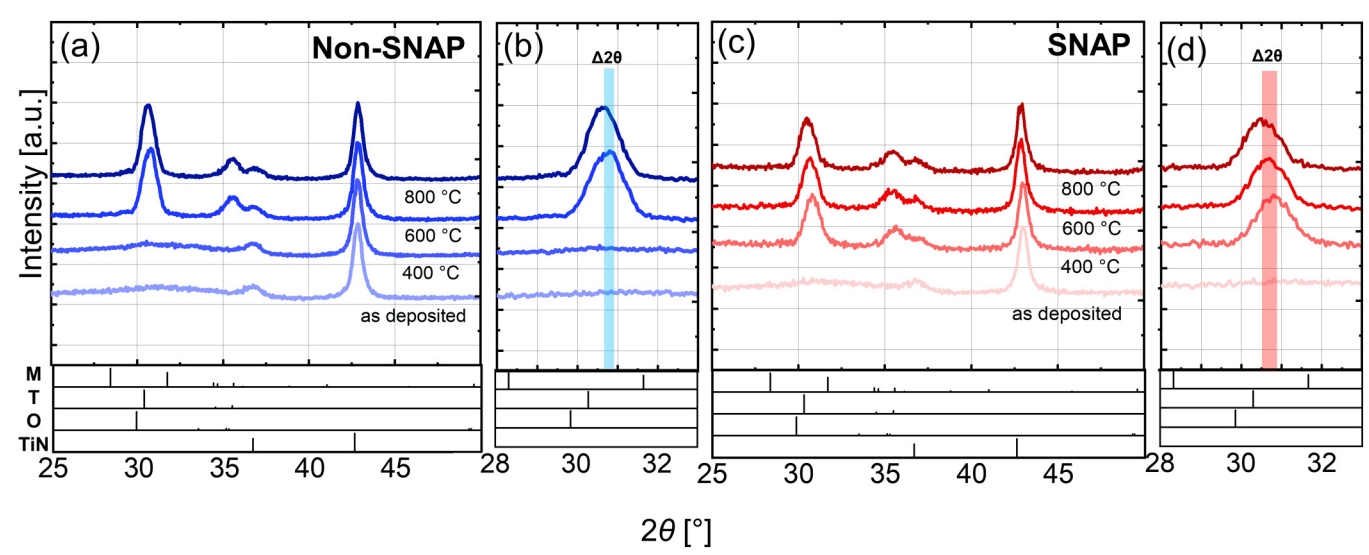


FIG. 4. GIXRD patterns for TiN/HZO/TiN capacitor stacks as-deposited and annealed at 400, 600, or 800 °C (a) and (b) fabricated via non-SNAP and (c) and (d) SNAP. Note that XRD patterns are normalized to the integrated peak of their (002) TiN reflection. The reference XRD patterns of HZO phases demarcated in the bottom panels are monoclinic (m) (PDF # 04-004-3850), orthorhombic (o) (PDF #: 04-005-5597), and tetragonal (t) (PDF #: 04-011-8820).

mixture. 28,31 ToF-SIMS confirmed the presence of a carbon interfacial layer. Such a non-ferroelectric layer is known to have pronounced effects on both the coercive field (Ec) and the tilt of the P-E loop. 27,32,33 Tagantsev et al. showed that the pinching and tilt of the hysteresis loop in bulk ceramics could be used as an indirect way to assess the thickness of a passive layer residing between the ferroelectric layer and electrode, where the passive layer is related to the slope of the P-E loop via the following relationship:

$$\frac{d}{L\varepsilon_{\rm d}} \sim \frac{E_c \varepsilon_o}{P_r}.\tag{1}$$

In Eq. (1), d is the thickness of the passive layer, L is the thickness of the ferroelectric layer,  $E_c$  is the coercive field,  $\varepsilon_d$  is the relative permittivity of the passive layer, and  $\varepsilon_0$  is the vacuum permittivity.<sup>27</sup> The downward tilting of the P-E loop and lower E<sub>c</sub> in the case of the non-SNAP capacitor suggests the presence of a thicker passivating layer at the HZO/TiN interface according to the Tagantsev et al. model. Applying Eq. (1) to the HZO thin film, the thickness of the passive layer was calculated to be 1.3 nm and 1.0 nm for non-SNAP and SNAP capacitors, respectively. The higher estimated dead layer thickness in non-SNAP suggests that exposure to ambient air after each layer deposition, specifically after the bottom TiN electrode deposition, leads to a thicker interfacial layer consistent with ToF-SIMS findings from Fig. 2.

Figure 4(b) leakage current density vs electric field (I-E) measurements show that SNAP-fabricated capacitors possess an overall lower leakage current density, especially at high electric fields above 1.0 MV/cm. The higher leakage current density in non-SNAP is attributed to a higher carbon concentration where carbon impurities have been found to form ~0.8 eV trap levels below the at 400, 600, or 800 °C (a) and (b) fabricated via non-SNAP and (c) and (d) SNAP. tion. The reference XRD patterns of HZO phases demarcated in the bottom panels tetragonal (t) (PDF #: 04-011-8820).

conduction band edge of HfO<sub>2</sub>, which likely leads to higher leakage current. The reference XRD patterns of HZO phases demarcated in the bottom panels tetragonal (t) (PDF #: 04-011-8820).

conduction band edge of HfO<sub>2</sub>, which likely leads to higher leakage current. Increased carbon-based impurities in HfO<sub>2</sub> thin films can also decrease the average grain size, resulting in higher grain boundary density, which acts as leakage conduction pathways. Thus, maintaining vacuum during ALD processing can control the leakage current density found in ferroelectric HZO films. Note that the non-SNAP capacitor demonstrated a higher control the leakage current density found in ferroelectric HZO films. Note that the non-SNAP capacitor demonstrated a higher breakdown strength in the negative bias region. Schenk *et al.* showed that a strong built-in bias exists in capacitors that suffer with the wake-up effect. Consistent with the characteristics of the non-SNAP capacitor, the enhanced breakdown strength may be related to the higher built-in bias in non-SNAP given the prevalence of tetragonal phase and its relation to wake-up.

To determine the root cause of the pinched P–E loop in non-SNAP-fabricated capacitor, non-SNAP and SNAP capacitors were heated from 25 to 175 °C and P–E measurements were acquired after a 10-min stabilization period for each temperature. Figures 6(a) and 6(b) show the P–E and J–E response as a function of temperature for the non-SNAP- and SNAP-fabricated capacitors, and some content of temperature for the non-SNAP- and SNAP-fabricated capacitors, and some content of the some con

of temperature for the non-SNAP- and SNAP-fabricated capacitors, respectively. Though both capacitors demonstrate a similar ±P<sub>r</sub> change as a function of temperature ( $\Delta P_r \sim 3.5-4 \,\mu\text{C/cm}^2$ ), the SNAP capacitor maintains a classical ferroelectric P-E loop shape while the non-SNAP capacitor progressively becomes more pinched with increasing temperature. The position of the switching current peaks, which correspond to the coercive field, is extracted from Fig. 6 and is plotted separately as a function of temperature in Fig. S5 in the supplementary material. For the SNAP-fabricated capacitor, the coercive field is stable with temperature. All four switching peaks of the non-SNAP-fabricated capacitor shift toward higher magnitudes of the electric field, consistent with the behavior of an antiferroelectric (AFE) material.

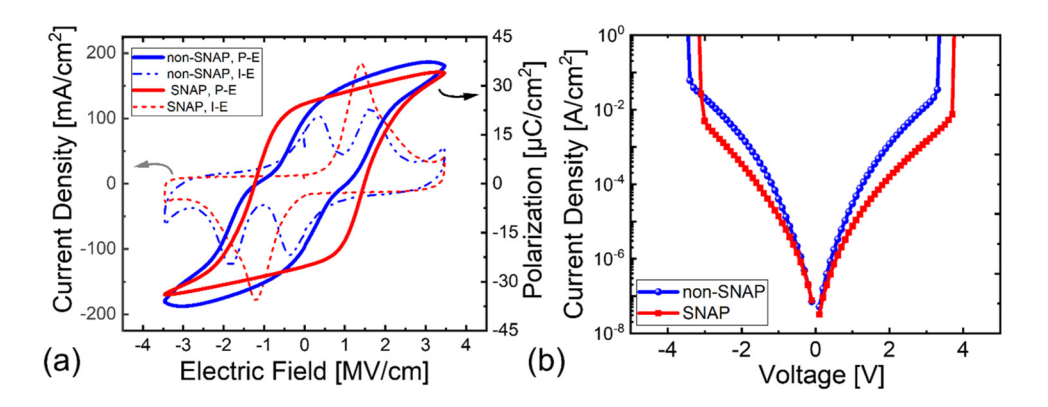


FIG. 5. Room-temperature electrical properties of non-SNAP- (blue) and SNAP-fabricated (red) TiN/HZO/TiN capacitors annealed at 800 °C. (a) Polarization vs electric field (P-E) and current density vs electric field (J-E), and (b) leakage current density vs voltage.

AFE materials possess a crystal structure with antiparallel dipoles, which allows the material to undergo an electricfield-induced phase transition between a non-polar AFE phase and a polar FE phase. Phenomenologically, AFE materials are identified by their double P-E loops where a critical electric field E<sub>F</sub> is required to induce the FE state; in the context of this study, we consider the tetragonal phase as the AFE phase. Pinched P-E loops may also be termed "antiferroelectric-like (AFE-like)," where P-E behavior appears AFE in the pristine state, but the P-E loop gradually de-pinches with field cycling or heat treatment into the FE state. For example, electric field cycling can cause defects to become redistributed, while heating can cause the relaxation of domain walls.<sup>36–38</sup> These two effects can lead to de-pinning as defects become more mobilized and redistribute uniformly across the material; the uninhibited domain walls allow for more effective ferroelectric switching.

Both mechanisms lead to a macroscopic de-pinching of the hysteresis loop.

While the AFE-like behavior observed in non-SNAP capacitors could originate from pinned domains from a higher defect concentration, the pinched P-E loop of non-SNAP may also originate from an intrinsic crystal structure possessing antiparallel of dipole ordering consistent with an AFE phase. In fact, Xu et al. posited that a pinched hysteresis in defect-free ferroelectrics could be a possible or the control of the control

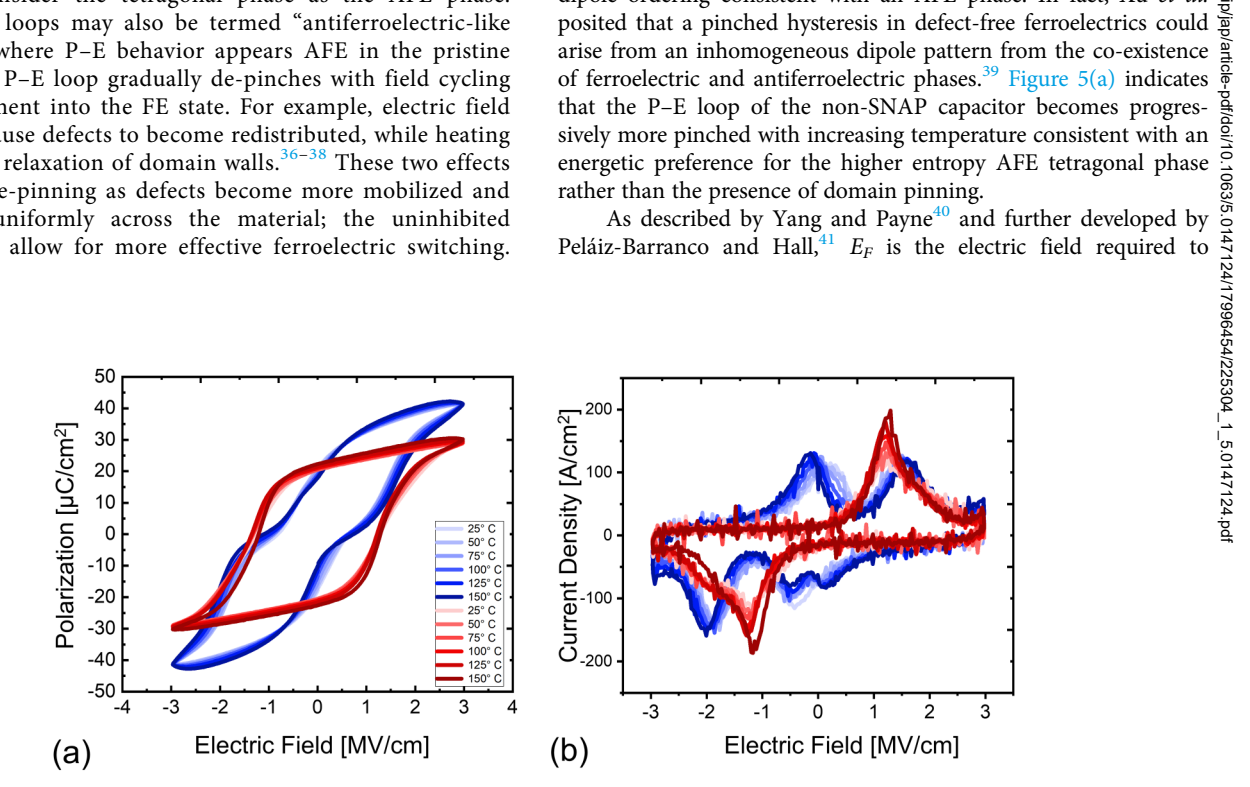


FIG. 6. Temperature-dependent electrical properties (a) P-E and (b) J-E, measured from 25 to 175 °C for TiN/HZO/TiN capacitors fabricated for non-SNAP (blue) and SNAP (red).

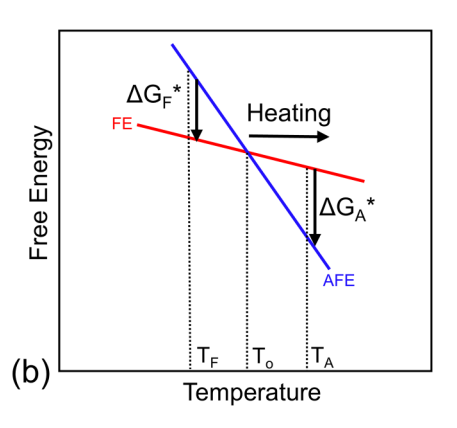


FIG. 7. (a) Schematic of an ideal AFE double P-E loop showing roomtemperature coercive fields, EA and EB and the expected coercive field shift with increased temperature, E'A and E'<sub>F</sub> (b) Energetic landscape of an AFE and FE material where heating promotes the energetic preference for the AFE phase above temperature To.

induce the AFE to FE transformation and is a sum of the intrinsic anhysteretic term,  $E_o$ , and the hysteretic term  $\Delta E_F$ ,

$$E_F = E_o + \Delta E_F. \tag{2}$$

Similarly,  $E_A$  is the electric field required to return to the FE phase from the AFE phase and is the difference between  $E_o$  and the hysteretic term  $\Delta E_A$ ,

$$E_A = E_o - \Delta E_A. \tag{3}$$

The value of  $E_o$  depends on the difference in free energy between the FE and AFE states, while  $\Delta E_F$  and  $\Delta E_A$  are determined by the transformational energy barriers between the AFE to FE states and vice versa, respectively. Theoretically,  $E_o$  should increase with temperature due to the entropy contribution of the AFE phase as the free energy difference between the AFE and FE become larger upon heating. Figure 7(a) schematically shows AFE behavior as represented in a P-E loop. When the temperature is increased, the coercive fields  $E_F$  and  $E_A$  shift toward  $E_F$  and  $E_A$ . Figure 7(b) illustrates the energy landscape of the AFE and FE phase where  $\Delta G_F^*$  and  $\Delta G_A^*$  are the free energy difference between the AFE and FE phase before and after To, respectively. T<sub>E</sub> is the temperature in which the FE phase possesses a lower ΔG and is energetically more preferred, To is the temperature at which the AFE and FE phases are energetically equivalent, and TA is a temperature at which  $\Delta G$  becomes lower for the AFE phase. Given the pinched P-E loop and double switching peak of the non-SNAP capacitor at room temperature, the free energy likely lies between To and TA where the presence of a room-temperature stable AFE phase is preferred. At higher temperatures, the free energy is further lowered for the AFE phase to a point closer to TA, which leads to the macroscopically observed shift of EA and EF toward a higher electric field. In other words, at higher temperatures, the AFE phase becomes energetically more favorable and, therefore, the barrier to induce the AFE to FE phase transformation,  $E_F$  increases in magnitude causing a macroscopic shift of the switching current peaks toward higher electric fields.

Several examples from the literature support the correlation of a macroscopically observed pinched P-E loop with the presence of an energetically favored anti-ferroelectric phase with increasing

temperature. Though doped HfO<sub>2</sub> thin films fabricated from ALD are not defect-free, many studies have confirmed that different orthorhombic and tetragonal phases co-exist within the film and lead to an observed pinched P-E loop. 10,28,42 Park et al. showed that P-E loops of Si:HfO2 films became progressively pinched or AFE-like with increasing temperature, concurrent with a reduced o111 and o110 peak intensity in GIXRD, suggesting a preference for the tetragonal phase. 42 Schroeder et al. also correlated a decrease in P<sub>r</sub> with an increase in tetragonal phase composition in PZO.<sup>23</sup> These findings are consistent with Lomenzo *et al.* who showed numerically that when 50% tetragonal phase is introduced by into a ferroelectric HfO<sub>2</sub> film, the ferroelectric hysteresis transforms to an antiferroelectric P-E loop.<sup>28</sup> Most recently, a reversible transifilms. These aforementioned studies are consistent with the observed energetic preference of the AFE tetragonal phase with increasing temperature in non-SNAP fabricate. increasing temperature in non-SNAP-fabricated capacitors shown in Fig. 6(a). The increase in AFE to FE phase transformation energy barrier with temperature is likely attributed to a macroenergy barrier with temperature is likely attributed to a macroscopic lattice strain due to thermal expansion, which alters the internal energy between the two phases, favoring the higher entropy AFE phase. At higher temperatures, the FE to AFE phase transformation possesses a lower formation energy, leading to the macroscopically observed increase of pinching in the P-E loop with increasing temperature.

Unlike the behavior of the non-SNAP-fabricated capacitor, the SNAP-fabricated capacitor showed a  $+|P_r|$  increase from 20 to  $\frac{24}{24}$   $\mu$ C/cm<sup>2</sup> from 25 to 150 °C in Fig. 5(b). It should be noted that  $\frac{72}{24}$ in classical ferroelectric systems, e.g., BaTiO $_3$ , PZT, the intrinsic  $\frac{\tau}{2}$ contribution to spontaneous polarization decreases as temperature increases in accordance with Landau-Ginzburg-Devonshire theory. observed increase in remanent polarization SNAP-fabricated HZO capacitors is likely a result of extrinsic contributions to polarization switching including, e.g., (1) an enhancement of thermally activated domain wall motion, 35,37 (2) increase in charged defect mobility, 44,45 and/or (3) domain de-pinning. 36 It is well-known that domain wall motion is a thermally activated process in ferroelectric films; as temperature increases, it is expected that both the barrier to switching decreases and the number of participating domains increases resulting in a lower coercive field  $(\pm E_c)$  and higher remanent polarization  $(\pm P_r)$ ,

respectively. Figure 6(b) shows that with increasing temperature in the present samples, the switching peak intensities increase, and the two peaks move slightly closer together toward a lower  $|\pm E_c|$ , consistent with an increase in switching contribution. Note, however, that the change in the coercive field is only slight compared to other classical ferroelectric materials, <sup>37,41</sup> suggesting that domain wall motion in HZO is not as thermally sensitive. Lee *et al.* suggested that the thickness of domain walls in HZO are vanishingly thin and, therefore, are energetically inefficient, moving only by hopping over a large energy barrier, <sup>46</sup> consistent with our observation of thermally insensitive domain walls in SNAP-fabricated HZO films.

In addition to P–E measurements leakage current density vs electric field (I–E) measurements were also acquired as a function of temperature to better assess the temperature stability and defect concentration in both films. Figure S6 shows the I–E plots as a function of temperature for HZO capacitors fabricated with and without vacuum breaking steps with an inset of current density as a function of temperature taken at ±2 V. In both cases, I–E measurements show an increase in the leakage tail at high fields (±3 V), suggesting temperature-enhanced charge injection contributions to leakage current. The higher magnitude lower leakage current at all temperatures compared to the non-SNAP-fabricated capacitor. The higher magnitude current density in non-SNAP-fabricated capacitors likely stems from increased carbon impurities consistent with observations made from ToF-SIMS and XPS analysis.

The temperature-dependent P–E measurements reveal that vacuum breaking during ALD leads to an energetically preferred AFE tetragonal phase in TiN/HZO/TiN capacitors relative to capacitors fabricated via vacuum-maintaining ALD process. The origin of an energetic preference for the AFE tetragonal phase composition in the non-SNAP-fabricated capacitor may stem from: (1) a higher concentration of carbon impurities that have been shown to preferentially stabilize the tetragonal phase in HfO<sub>2</sub> films  $^{49,50}$  and/or (2) an increased depolarization field expected for a thicker dead layer interface that decreases the stability of the ferroelectric orthorhombic phase.  $^{28}$  In contrast, temperature-dependent P–E measurements of SNAP-fabricated capacitors showed an increase in  $\pm |\mathrm{P_r}|$  and a decrease in  $\pm |\mathrm{E_c}|$ , attributable to either enhanced domain wall motion and/or domain de-pinning.

The effect of breaking vacuum on the fatigue properties of TiN/HZO/TiN capacitors is investigated by examining the evolution of P-E and permittivity-electric field measurements as a function of electric field cycling. P-E loops as a function of electric field cycling are shown in Figs. 8(a) and 8(b) and were extracted from the 3.0 MV/cm endurance measurement in Fig. 8(c). P-E loops of the non-SNAP-fabricated capacitor in Fig. 8(a) gradually become less pinched with field cycling, i.e., ±Ec increases, accompanied by a modest increase in  $\pm |P_r|$  with electric field cycling. The overlaying current density vs electric field measurements in Fig. 8(a) show that the back-switching peaks move toward the coercive field until they merge with the forward-switching peaks after 10<sup>4</sup> switching cycles have been applied. After 10<sup>4</sup> cycles, the fully "woken-up" state is achieved in the non-SNAP capacitor. The gradual opening of the P-E loop and merging of the switching peaks with increased cycling is consistent with the wake-up phenomenon. Five major

mechanisms are typically cited as possible origins of wake-up: phase transformation due to defect distribution, domain pinning/ depinning pinned from the field-driven redistribution of defects, charge injection, ferroelastic switching, and/or interfacial breakdown. 30,51-53 However, given evidence for a significant portion of the tetragonal phase in the non-SNAP capacitor from GIXRD analysis and temperature-dependent P-E measurements, the observed de-pinching of the P-E loop as a function of electric field cycling is likely due to a field-induced phase transition. In contrast, the shape of the P-E loops for the SNAP capacitor in Fig. 8(b) stays relatively constant with electric field cycling, suggesting negligible wake-up. After 10<sup>4</sup> cycles, however, the P<sub>r</sub> value begins to decrease, suggesting the onset of fatigue from domain pinning by defect generation and accumulation 45,54 seed-inhibition mechanism.<sup>55</sup> The endurance measurement in Fig. 8(c) shows that the SNAP-fabricated capacitor undergoes dielectric breakdown at  $5 \times 10^5$  cycles, whereas the non-SNAP-fabricated capacitor survives for 109 cycles at a cycling field of 3.0 MV/cm. At a cycling field of 3.5 MV/cm, the fatigue limit of the non-SNAP and SNAP-fabricated capacitor was measured to be  $\sim 1 \times 10^9$  cycles and  $\sim 7 \times 10^5$  cycles, respectively. The observed increase in polarization with progressive field cycling in both capacitors is consistent with charge injection which may stem from the nearby electrode during ferroelectric switching at high applied  $\frac{\sigma}{\omega}$ 

The enhanced endurance of the non-SNAP capacitor likely stems from two factors: (1) a slight voltage drop caused by the interfacial layer which reduces the macroscopic electric field experienced by the ferroelectric and/or (2) the presence of a higher relative fraction of tetragonal phase, which transforms to the orthorhombic phase during electric field cycling. Given the observed presence of the wake-up effect in the non-SNAP capacitor accompanied by a gradual de-pinching of the P–E loop and increase in P<sub>r</sub> as a function of electric field cycling, it is more likely that the higher endurance in the non-SNAP-fabricated capacitor is due to a larger fraction of tetragonal phase, which decreases the P<sub>r</sub> and subsequently prevents charge injection. To Our observation here is consistent with other HZO capacitor systems that contain intentionally inserted, sub-nanometer LaO<sub>x</sub> or AlO<sub>x</sub> interlayers, which were also found to improve field cycling endurance.

To further aid in discerning the phase evolution with electric field cycling, permittivity measurements were conducted as a function of electric field cycling. Small-signal capacitance measurements were transformed to the permittivity vs DC bias field ( $\epsilon_r$ –E) plots shown in Fig. 8(d). Permittivity as a function of the DC bias field is known to be sensitive to a combination of intrinsic (i.e., lattice) and extrinsic (e.g., domain wall, defects) contributions and can be de-convoluted, at least partially, by observing the response at the saturating and coercive field, respectively.  $\epsilon_r$ –E loops of the SNAP-fabricated capacitor (red) show a classic butterfly shape in both the pristine and cycled state, while the non-SNAP capacitor (blue) shows a pinched loop in the virgin state, which opens up only after  $10^4$  cycles at a cycling field of 3.5 MV/cm. At the maximum DC bias fields of  $\pm 3$  MV/cm, only the intrinsic contribution of the lattice affects the permittivity and, therefore, the value of  $\epsilon_r$  near this field amplitude can be used to assess the film phase composition. A relative permittivity of 30 and 35–40 has been

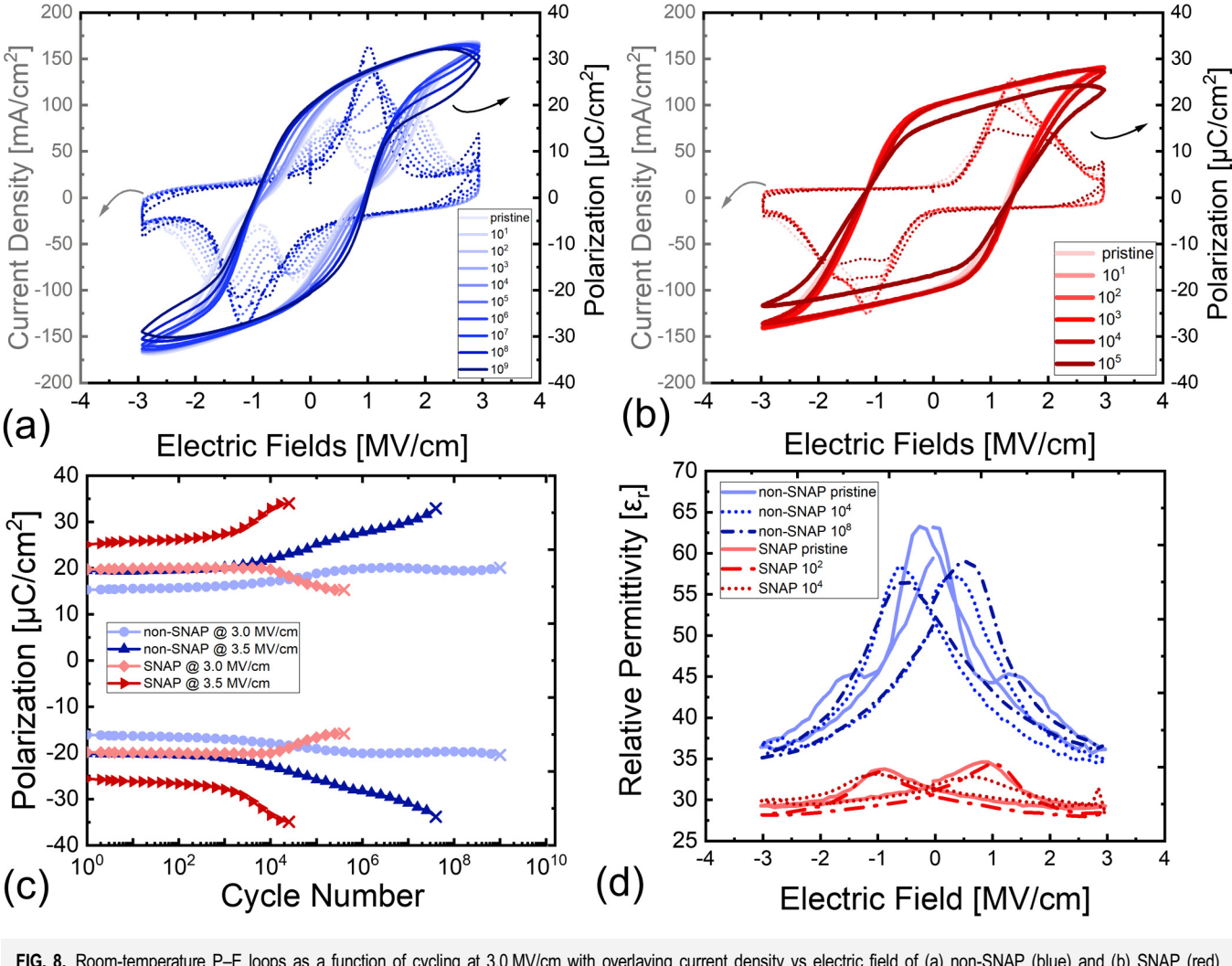


FIG. 8. Room-temperature P-E loops as a function of cycling at 3.0 MV/cm with overlaying current density vs electric field of (a) non-SNAP (blue) and (b) SNAP (red) TiN/HZO/TiN capacitors annealed at 800 °C for 30 s; (c) Cycling endurance measurement conducted at 3.0 and 3.5 MV/cm; (d) Small-signal permittivity vs electric field for pristine and cycled non-SNAP (blue) and SNAP (red) capacitors at 3.0 MV/cm.

previously reported for the orthorhombic and tetragonal phases, respectively. The  $\varepsilon_r$  at the maximum DC bias fields of  $\pm 3$  MV/cm are approximately  $\sim 37$  and  $\sim 30$  for the non-SNAP- and SNAP-fabricated capacitor, consistent with a predominately tetragonal and orthorhombic phase composition, respectively. The observed changes in the shape of the P–E and  $\varepsilon_r$ –E loops and differences in  $\varepsilon_r$  values with electric field cycling strongly suggest that the non-SNAP-fabricated capacitor experiences a wake-up effect characterized by a phase transformation from the tetragonal to the orthorhombic phase during field cycling. Though the pinched loop of non-SNAP becomes butterfly-shaped after  $10^8$  cycles at 3.0 MV/cm, the permittivity values at both the saturating ( $\pm 3$  MV/cm) and switching fields ( $\pm 1$  MV/cm) remain considerably higher than the SNAP-fabricated capacitor. The heightened permittivity values at saturating fields in non-SNAP, even after undergoing a field-induced

phase transformation, suggests that a considerable fraction of the tetragonal phase remains in the film even after field cycling. Overall, the electrical measurements as a function of electric field cycling indicate that vacuum breaking during ALD processing is directly correlated to increased cycling endurance and wake-up effect originating from carbon impurities at the interface which promotes a higher fraction of tetragonal phase in HZO film. As a result, preventing carbon contamination by maintaining vacuum during *in situ* ALD deposition of the TiN/HZO/TiN capacitor stack can enhance P<sub>r</sub> and avoid deleterious wake-up behavior.

## IV. CONCLUSIONS

In summary, the choice of maintaining or breaking vacuum during ALD strongly influences the chemical, structural, and

J. Appl. Phys. 133, 225304 (2023); doi: 10.1063/5.0147124

Published under an exclusive license by AIP Publishing

Downloaded from http://pubs.aip.org/aip/jap/article-pdf/doi/10.1063/5.0147124/17996454/225304\_

electrical properties of TiN/HZO/TiN capacitors. ToF-SIMS depth profiles indicate that vacuum breaking during ALD leads to the formation of a more pronounced interlayer mainly stemming from adsorbed carbon contamination. Increased carbon impurities in capacitors have several consequences on the structural properties, where differences in o111/t011 and o{002} peak intensities and permittivity measurements suggest differing relative orthorhombic and tetragonal phase fractions in capacitors made with and without vacuum breaking steps. A larger  $2\theta$  peak shift near  $\sim 30^{\circ}$  is observed for capacitors produced from the maintaining vacuummaintaining process and suggests a higher orthorhombic phase content consistent with the observed higher remanent polarization  $23 \,\mu\text{C/cm}^2$ . P–E measurements as a function of electric field cycling show that samples made with vacuum breaking steps experience a gradual increase in Pr and de-pinching with electric field cycling, indicating that vacuum breaking ALD fabrication generates HZO films possessing the deleterious wake-up phenomenon. Changes in the shape and the gradual de-pinching of the  $\varepsilon_{r}$  E loops in the vacuum breaking ALD sample are consistent with a wake-up effect caused by the incorporation of carbon impurities, which preferentially stabilize the tetragonal phase in the pristine state. The results presented here suggest that vacuum should be maintained during ALD of TiN/HZO/TiN capacitor stacks to minimize adventitious carbon impurities to effectively mitigate the wake-up effect in HZO capacitors. On the other hand, our results also reveal that interfacial layers generated by breaking vacuum can also improve field cycling endurance. Future work should consider artificially inserted interlayers within the TiN/HZO/TiN capacitor stack to balance the desired remanent polarization, leakage density, endurance, and reliability.

## SUPPLEMENTARY MATERIAL

The supplementary material contains additional experimental details on the XPS, TOF-SIMS, TEM, and GIXRD measurements. Also included in the supplemental information are EDS maps of SNAP- and non-SNAP-fabricated capacitors; TOF-SIMS species ratios at the top interface of SNAP and non-SNAP-fabricated capacitors; P-E and J-E measurements of SNAP and non-SNAP capacitors annealed at 400 and 600 °C; switching current density vs electric field measurements for SNAP and non-SNAP capacitors; and leakage current density as a function of the temperature for SNAP and non-SNAP capacitors.

# **ACKNOWLEDGMENTS**

This contribution is based upon the work supported by the National Science Foundation (NSF), as part of the Center for Dielectrics and Piezoelectrics under Grant Nos. IIP-1841453 and IIP-1841466. A.H. was supported by the National Science Foundation Graduate Research Fellowship Program (No. DGE-1746939), NSF INTERN supplemental grant, and the IIE-GIRE Program funded by the National Science Foundation (No. 1829436). This work was performed at the Analytical Instrumentation Facility (AIF) at North Carolina State University and at the NC State Nanofabrication Facility (NNF), both of which are supported by the State of North Carolina and the National Science Foundation (Award No. ECCS-2025064). AIF and NNF are

members of the North Carolina Research Triangle Nanotechnology Network (RTNN), a site in the National Nanotechnology Coordinated Infrastructure (NNCI). P.D.L., R.A., and B.X. acknowledge the support by the Deutsche Forschungs Gemeinschaft DFG within the following projects [Zeppelin (No. 433647091) and HOMER (No. 430054035)]. U.S. and T.M. were financially supported out of the Saxonian State budget approved by the delegates of the Saxon State Parliament.

## **AUTHOR DECLARATIONS**

## **Conflict of Interest**

The authors have no conflicts to disclose.

## **Author Contributions**

A.H. and Y.L. contributed equally to this work.

A.H. and Y.L. contributed equally to this work.

Alex Hsain: Conceptualization (equal); Data curation (equal); Funding acquisition (equal); Investigation (equal); Validation (equal); Visualization (equal); Writing – original draft (equal). (equal); Visualization (equal); Writing - original draft (equal). Younghwan Lee: Conceptualization (equal); Investigation (equal); Methodology (equal); Visualization (equal); Writing – review & editing (equal). Patrick D. Lomenzo: Data curation (equal); Project administration (equal); Resources (equal); Supervision (equal); Writing – review & editing (equal). Ruben Alcala:

Methodology (equal); Resources (equal); Writing – review & editing (equal). editing (equal). Bohan Xu: Data curation (equal); Methodology (equal); Writing - review & editing (equal). Thomas Mikolajick: Investigation (equal); Project administration (equal); Resources (equal); Supervision (equal); Writing – review & editing (equal). Uwe Schroeder: Investigation (equal); Project administration (equal); Resources (equal); Supervision (equal); Writing – review & editing (equal). Gregory N. Parsons: Project administration (equal); Supervision (equal); Writing – review & editing (equal). Jacob L. Jones: Funding acquisition (equal); Investigation (equal); Project administration (equal); Resources (equal); Supervision (equal); Writing – review & editing (equal).

DATA AVAILABILITY

The data that support the findings of this study are available from the corresponding authors upon reasonable request.

REFERENCES

1. S. Böscke, S. Teichert, D. Bräuhaus, J. Müller, U. Schröder, U. Böttger, and Uwe Schroeder: Investigation (equal); Project administration

<sup>1</sup>T. S. Böscke, S. Teichert, D. Bräuhaus, J. Müller, U. Schröder, U. Böttger, and T. Mikolajick, "Phase transitions in ferroelectric silicon doped hafnium oxide," Appl. Phys. Lett. 99(11), 112904 (2011).

<sup>2</sup>S. Mueller, J. Muller, R. Hoffmann, E. Yurchuk, T. Schlosser, R. Boschke, J. Paul, M. Goldbach, T. Herrmann, A. Zaka, U. Schroder, and T. Mikolajick, "From MFM capacitors toward ferroelectric transistors endurance and disturb characteristics of HfO2-based FeFET devices," IEEE Trans. Electron Devices 60(12), 4199-4205 (2013).

3C. Gattinoni, N. Strkalj, R. Härdi, M. Fiebig, M. Trassin, and N. A. Spaldin, "Interface and surface stabilization of the polarization in ferroelectric thin films," Proc. Natl. Acad. Sci. U.S.A. 117(46), 28589-28595 (2020).

<sup>4</sup>P. D. Lomenzo, Q. Takmeel, C. Zhou, C. M. Fancher, E. Lambers, N. G. Rudawski, J. L. Jones, S. Moghaddam, and T. Nishida, "Tan interface

properties and electric field cycling effects on ferroelectric Si-doped  $HfO_2$  thin films," J. Appl. Phys. 117(13), 134105 (2015).

- <sup>5</sup>E. O. Filatova, S. S. Sakhonenkov, A. S. Konashuk, and V. V. Afanas'ev, "Control of TiN oxidation upon atomic layer deposition of oxides," Phys. Chem. Chem. Phys. **20**(44), 27975–27982 (2018).
- <sup>6</sup>T. Szyjka, L. Baumgarten, T. Mittmann, Y. Matveyev, C. Schlueter, T. Mikolajick, U. Schroeder, and M. Müller, "Enhanced ferroelectric polarization in TiN/HfO<sub>2</sub>/TiN capacitors by interface design," ACS Appl. Electron. Mater. 2(10), 3152–3159 (2020).
- **7**S. S. Fields, S. W. Smith, C. M. Fancher, M. D. Henry, S. L. Wolfley, M. G. Sales, S. T. Jaszewski, M. A. Rodriguez, G. Esteves, P. S. Davids, S. J. McDonnell, and J. F. Ihlefeld, "Metal nitride electrode stress and chemistry effects on phase and polarization response in ferroelectric  $Hf_{0.5}Zr_{0.5}O_2$  thin films," Adv. Mater. Interfaces **8**(10), 2100018 (2021).
- <sup>8</sup>S. J. Kim, J. Mohan, S. R. Summerfelt, and J. Kim, "Ferroelectric  $Hf_{0.5}Zr_{0.5}O_2$  thin films: A review of recent advances," JOM 71(1), 246–255 (2019).
- <sup>9</sup>M. H. Park, Y. H. Lee, T. Mikolajick, U. Schroeder, and C. S. Hwang, "Review and perspective on ferroelectric HfO<sub>2</sub>-based thin films for memory applications," MRC 8(03), 795–808 (2018).
- <sup>10</sup>E. D. Grimley, T. Schenk, T. Mikolajick, U. Schroeder, and J. M. LeBeau, "Atomic structure of domain and interphase boundaries in ferroelectric HfO<sub>2</sub>," Adv. Mater. Interfaces 5(5), 1701258 (2018).
- <sup>11</sup>K. D. Kim, M. H. Park, H. J. Kim, Y. J. Kim, T. Moon, Y. H. Lee, S. D. Hyun, T. Gwon, and C. S. Hwang, "Ferroelectricity in undoped-HfO<sub>2</sub> thin films induced by deposition temperature control during atomic layer deposition," J. Mater. Chem. C 4(28), 6864–6872 (2016).
- <sup>12</sup>Y. Lee, H. Alex Hsain, S. S. Fields, S. T. Jaszewski, M. D. Horgan, P. G. Edgington, J. F. Ihlefeld, G. N. Parsons, and J. L. Jones, "Unexpectedly large remanent polarization of  $Hf_{0.5}Zr_{0.5}O_2$  metal–ferroelectric–metal capacitor fabricated without breaking vacuum," Appl. Phys. Lett. **118**(1), 012903 (2021).
- <sup>13</sup>J. Y. Kim, Y. Kim, and H. Jeon, "Characteristics of TiN films deposited by remote plasma-enhanced atomic layer deposition method," Jpn. J. Appl. Phys. 42(Part 2, No. 4B), L414–L416 (2003).
- <sup>14</sup>O. S. Yulmetova, M. S. Tutova, and R. F. Yulmetova, "Chemical analysis of thin-film's colour generation during surface laser oxidation of TiN-coating," J. Phys.: Conf. Ser. 1124, 081010 (2018).
- <sup>15</sup>W. Weinreich, A. Shariq, K. Seidel, J. Sundqvist, A. Paskaleva, M. Lemberger, and A. J. Bauer, "Detailed leakage current analysis of metal-insulator-metal capacitors with ZrO<sub>2</sub>, ZrO<sub>2</sub>/SiO<sub>2</sub> /ZrO<sub>2</sub>, and ZrO<sub>2</sub>/Al<sub>2</sub>O<sub>3</sub>/ZrO<sub>2</sub> as dielectric and TiN electrodes," J. Vac. Sci. Technol. B **31**(1), 01A109 (2013).
- <sup>16</sup>L. Xu, T. Nishimura, S. Shibayama, T. Yajima, S. Migita, and A. Toriumi, "Ferroelectric phase stabilization of HfO<sub>2</sub> by nitrogen doping," Appl. Phys. Express 9(9), 091501 (2016).
- 17½. P. Londhe, A. Gupta, N. Ponpandian, D. Kumar, and V. R. Reddy, "TiO<sub>2</sub> as diffusion barrier at Co/AlQ<sub>3</sub> interface studied by x-Ray standing wave technique," J. Phys. D: Appl. Phys. 51(22), 225303 (2018).
- <sup>18</sup>P. Alén, M. Vehkamäki, M. Ritala, and M. Leskelä, "Diffusion barrier properties of atomic layer deposited ultrathin Ta2O5 and TiO2 films," J. Electrochem. Soc. 153, G304 (2006).
- 19 M. H. Park, H. J. Kim, G. Lee, J. Park, Y. H. Lee, Y. J. Kim, T. Moon, K. D. Kim, S. D. Hyun, H. W. Park, H. J. Chang, J.-H. Choi, and C. S. Hwang, "A comprehensive study on the mechanism of ferroelectric phase formation in hafnia-zirconia nanolaminates and superlattices," Appl. Phys. Rev. 6(4), 041403 (2019).
- <sup>20</sup>M.-Y. Ho, H. Gong, G. D. Wilk, B. W. Busch, M. L. Green, P. M. Voyles, D. A. Muller, M. Bude, W. H. Lin, A. See, M. E. Loomans, S. K. Lahiri, and P. I. Räisänen, "Morphology and crystallization kinetics in HfO<sub>2</sub> thin films grown by atomic layer deposition," J. Appl. Phys. 93(3), 1477–1481 (2003).
- grown by atomic layer deposition," J. Appl. Phys. **93**(3), 1477–1481 (2003). <sup>21</sup>A. J. Lee, B. S. Kim, J. H. Hwang, Y. Kim, H. Oh, Y. Park, and W. Jeon, "Controlling the crystallinity of HfO<sub>2</sub> thin film using the surface energy-driven phase stabilization and template effect," Appl. Surf. Sci. **590**, 153082 (2022). <sup>22</sup>H. A. Hsain, Y. Lee, G. Parsons, and J. L. Jones, "Compositional dependence
- $^{-}$ H. A. Hsain, Y. Lee, G. Parsons, and J. L. Jones, "Compositional dependence of crystallization temperatures and phase evolution in hafnia-zirconia (Hf<sub>x</sub> Zr<sub>1</sub>  $_{-x}$ )O<sub>2</sub> thin films," Appl. Phys. Lett. **116**(19), 192901 (2020).

- <sup>23</sup>U. Schroeder, T. Mittmann, M. Materano, P. D. Lomenzo, P. Edgington, Y. H. Lee, M. Alotaibi, A. R. West, T. Mikolajick, A. Kersch, and J. L. Jones, "Temperature-dependent phase transitions in  $Hf_xZr_{1-x}O_2$  mixed oxides: Indications of a proper ferroelectric material," Adv. Elect. Mater. 116, 2200265 (2022).
- <sup>24</sup>C. Künneth, R. Materlik, M. Falkowski, and A. Kersch, "Impact of four-valent doping on the crystallographic phase formation for ferroelectric HfO<sub>2</sub> from first-principles: Implications for ferroelectric memory and energy-related applications," ACS Appl. Nano Mater. 1(1), 254–264 (2018).
- 25 G. Esteves, K. Ramos, C. Fancher, and J. Jones, LIPRAS (Line-Profile Analysis Software) (2017).
- **26**Y. Lee, R. A. Broughton, H. A. Hsain, S. K. Song, P. G. Edgington, M. D. Horgan, A. Dowden, A. Bednar, D. H. Lee, G. N. Parsons, M. H. Park, and J. L. Jones, "The influence of crystallographic texture on structural and electrical properties in ferroelectric  $Hf_{0.5}Zr_{0.5}O_2$ ." J. Appl. Phys. **132**(24), 244103 (2022). **27**A. K. Tagantsev, M. Landivar, E. Colla, and N. Setter, "Identification of
- <sup>2</sup> A. K. Tagantsev, M. Landivar, E. Colla, and N. Setter, "Identification of passive layer in ferroelectric thin films from their switching parameters," J. Appl. Phys. **78**(4), 2623–2630 (1995).
- <sup>28</sup>P. D. Lomenzo, C. Richter, T. Mikolajick, and U. Schroeder, "Depolarization as driving force in antiferroelectric hafnia and ferroelectric wake-up," ACS Appl. Electron. Mater. **2**(6), 1583–1595 (2020).
- T. Schenk, M. Hoffmann, J. Ocker, M. Pešić, T. Mikolajick, and U. Schroeder, "Complex internal bias fields in ferroelectric hafnium oxide," ACS Appl. Mater. Interfaces 7(36), 20224–20233 (2015).
- <sup>30</sup>J. F. Scott and M. Dawber, "Oxygen-vacancy ordering as a fatigue mechanism in perovskite ferroelectrics," Appl. Phys. Lett. **76**(25), 3801–3803 (2000).
- 31. E. D. Grimley, T. Schenk, X. Sang, M. Pešić, U. Schroeder, T. Mikolajick, and 5. J. M. LeBeau, "Structural changes underlying field-cycling phenomena in ferroelectric HfO<sub>2</sub> thin films," Adv. Electron. Mater. **2**(9), 1600173 (2016).
- 32B. Chen, H. Yang, L. Zhao, J. Miao, B. Xu, X. G. Qiu, B. R. Zhao, X. Y. Qi, and X. F. Duan, "Thickness and dielectric constant of dead layer in Pt/(Ba<sub>0.7</sub>Sr<sub>0.3</sub>)TiO<sub>3</sub>/YBa<sub>2</sub>Cu<sub>3</sub>O<sub>7-x</sub> capacitor," Appl. Phys. Lett. 84(4), 583–585 (2004).
- 33Y. Podgorny, V. Vorotilov, K. A. Sigov, A. S. Scott, and J. F, "Dead layer thickness estimation at the ferroelectric film-metal interface in PZT," Appl. Phys. Lett. 114(13), 132902 (2019).
- $^{34}$ M.-J. Choi, H.-H. Park, D. S. Jeong, J. H. Kim, J.-S. Kim, and S. K. Kim,  $^{84}$ Mtomic layer deposition of HfO<sub>2</sub> thin films using H<sub>2</sub>O<sub>2</sub> as oxidant," Appl. Surf.  $^{95}$ Sci. 301, 451-455 (2014).
- 35K. D. Kim, Y. H. Lee, T. Gwon, Y. J. Kim, H. J. Kim, T. Moon, S. D. Hyun, H. W. Park, M. H. Park, and C. S. Hwang, "Scale-up and optimization of HfO<sub>2</sub>-ZrO<sub>2</sub> solid solution thin films for the electrostatic supercapacitors," Nano Energy 39, 390–399 (2017).
- 36F. P. G. Fengler, M. Pešić, S. Starschich, T. Schneller, C. Künneth, U. Böttger, B. H. Mulaosmanovic, T. Schenk, M. H. Park, R. Nigon, P. Muralt, T. Mikolajick, and U. Schroeder, "Domain pinning: Comparison of hafnia and PZT based ferroelectrics," Adv. Electron. Mater. 3(4), 1600505 (2017).
- <sup>37</sup>F. Xu, S. Trolier-McKinstry, W. Ren, B. Xu, Z.-L. Xie, and K. J. Hemker, Domain wall motion and Its contribution to the dielectric and piezoelectric properties of lead zirconate titanate films, J. Appl. Phys. **89**(2), 1336–1348 (2001).
- <sup>38</sup>M. Pešić, F. P. G. Fengler, L. Larcher, A. Padovani, T. Schenk, E. D. Grimley, X. Sang, J. M. LeBeau, S. Slesazeck, U. Schroeder, and T. Mikolajick, "Physical mechanisms behind the field-cycling behavior of HfO<sub>2</sub>-based ferroelectric capacitors," Adv. Funct. Mater. 26(25), 4601–4612 (2016).
- <sup>39</sup>B. Xu, C. Paillard, B. Dkhil, and L. Bellaiche, "Pinched hysteresis loop in defect-free ferroelectric materials," Phys. Rev. B **94**(14), 140101 (2016).
- <sup>40</sup>P. Yang and D. A. Payne, "Thermal stability of field-forced and field-assisted antiferroelectric-ferroelectric phase transformations in Pb(Zr,Sn,Ti)O<sub>3</sub>," J. Phys. Appl. 71, 1361 (1992).
- Appl. 71, 1361 (1992).

  <sup>41</sup>A. Pelaiz-Barranco and D. A. Hall, "Influence of composition and pressure on the electric field-induced antiferroelectric to ferroelectric phase transformation in lanthanum modified lead zirconate titanate ceramics," IEEE Trans Ultrason Ferroelectr Freq Control 56(9), 1785–1791 (2009).

- <sup>42</sup>M. H. Park, C. Chung, T. Schenk, C. Richter, M. Hoffmann, S. Wirth, J. L. Jones, T. Mikolajick, and U. Schroeder, "Origin of temperature-dependent ferroelectricity in Si-doped HfO2," Adv. Electron. Mater. 4(4), 1700489 (2018). 43Y. Cheng, Z. Gao, K. H. Ye, H. W. Park, Y. Zheng, Y. Zheng, J. Gao, M. H. Park, J.-H. Choi, K.-H. Xue, C. S. Hwang, and H. Lyu, "Reversible transition between the polar and antipolar phases and its implications for wake-up and fatigue in HfO2-based ferroelectric thin film," Nat. Commun. 13(1), 645 (2022).
- 44E. Cartier and A. Kerber, "Stress-induced leakage current and defect generation in NFETs with HfO2/TiN gate stacks during positive-bias temperature stress," in 2009 IEEE International Reliability Physics Symposium, Montreal, QC, Canada (IEEE, 2009), pp. 486-492.
- 45 F. Huang, X. Chen, X. Liang, J. Qin, Y. Zhang, T. Huang, Z. Wang, B. Peng, P. Zhou, H. Lu, L. Zhang, L. Deng, M. Liu, Q. Liu, H. Tian, and L. Bi, "Fatigue mechanism of yttrium-doped hafnium oxide ferroelectric thin films fabricated
- by pulsed laser deposition," Phys. Chem. Chem. Phys. 19(5), 3486–3497 (2017). 46H.-J. Lee, M. Lee, K. Lee, J. Jo, H. Yang, Y. Kim, S. C. Chae, U. Waghmare, and J. H. Lee, "Scale-free ferroelectricity induced by flat phonon bands in HfO2," Science 369(6509), 1343-1347 (2020).
- 47M. Pešić, C. Künneth, M. Hoffmann, H. Mulaosmanovic, S. Müller, E. T. Breyer, U. Schroeder, A. Kersch, T. Mikolajick, and S. Slesazeck, "A computational study of hafnia-based ferroelectric memories: From Ab initio via physical modeling to circuit models of ferroelectric device," J. Comput. Electron. 16(4), 1236-1256 (2017).
- 48D. R. Islamov, V. A. Gritsenko, T. V. Perevalov, V. A. Pustovarov, O. M. Orlov, A. G. Chernikova, A. M. Markeev, S. Slesazeck, U. Schroeder, T. Mikolajick, and G. Y. Krasnikov, "Identification of the nature of traps involved in the field cycling of Hf<sub>0.5</sub>Zr<sub>0.5</sub>O<sub>2</sub>-based ferroelectric thin films," Acta Mater. 166, 47-55 (2019).
- 49 H.-S. Jung, S. H. Jeon, H. K. Kim, I.-H. Yu, S. Y. Lee, J. Lee, Y. J. Chung, D.-Y. Cho, N.-I. Lee, T. J. Park, J.-H. Choi, S. Han, and C. S. Hwang, "The impact of carbon concentration on the crystalline phase and dielectric constant

- of atomic layer deposited HfO 2 films on Ge substrate," ECS J. Solid State Sci. Technol. 1(2), N33-N37 (2012).
- 50 M. Choi, J. L. Lyons, A. Janotti, and C. G. Van de Walle, "Impact of carbon and nitrogen impurities in high-κ dielectrics on metal-oxide-semiconductor devices," Appl. Phys. Lett. 102(14), 142902 (2013).
- 51 M. Materano, P. D. Lomenzo, A. Kersch, M. H. Park, T. Mikolajick, and U. Schroeder, "Interplay between oxygen defects and dopants: Effect on structure and performance of HfO2-based ferroelectrics," Inorg. Chem. Front. 8(10), 2650-2672 (2021).
- 52S. S. Fields, S. W. Smith, S. T. Jaszewski, T. Mimura, D. A. Dickie, G. Esteves, M. David Henry, S. L. Wolfley, P. S. Davids, and J. F. Ihlefeld, "Wake-up and fatigue mechanisms in ferroelectric  $Hf_{0.5}Zr_{0.5}O_2$  films with symmetric  $RuO_2$ electrodes," J. Appl. Phys. 130(13), 134101 (2021).
- 53 T. Shimizu, T. Mimura, T. Kiguchi, T. Shiraishi, T. Konno, Y. Katsuya, O. Sakata, and H. Funakubo, "Ferroelectricity mediated by ferroelastic domain switching in HfO<sub>2</sub>-based epitaxial thin films," Appl. Phys. Lett. 113(21), 212901
- 54W. L. Warren, D. Dimos, B. A. Tuttle, G. E. Pike, R. W. Schwartz, P. J. Clews, and D. C. McIntyre, "Polarization suppression in Pb(Zr,Ti)O3 thin films," I. Appl. Phys. 77(12), 6695–6702 (1995).
- 55 E. L. Colla, D. V. Taylor, A. K. Tagantsev, and N. Setter, "Discrimination between bulk and interface scenarios for the suppression of the switchable polarization (fatigue) in Pb(Zr,Ti)O<sub>3</sub> thin films capacitors with Pt electrodes," Appl. Phys. Lett. 72(19), 2478-2480 (1998).
- 56R. Alcala, P. Mehmood, P. Vishnumurthy, T. Mittmann, T. Mikolajick, and U. Schroeder, "Influence of interfacial oxide layers in Hf<sub>0.5</sub>Zr<sub>0.5</sub>O<sub>2</sub> based ferroelectric capacitors on reliability performance," in 2022 IEEE International a Memory Workshop (IMW) (IEEE, 2022), pp. 1-4.
- electric capacitors on reliability performance," in 2022 IEEE International Fomemory Workshop (IMW) (IEEE, 2022), pp. 1–4.

  57M. Hyuk Park, H. Joon Kim, Y. Jin Kim, W. Lee, H. Kyeom Kim, and C. Seong Hwang, "Effect of forming Gas annealing on the ferroelectric properties of Hf<sub>0.5</sub>Zr<sub>0.5</sub>O<sub>2</sub> thin films with and without Pt electrodes," Appl. Phys. Lett. 102(11), 112914 (2013).